Deep Learning–Enabled Quantification of ^{99m}Tc-Pyrophosphate SPECT/CT for Cardiac Amyloidosis

Robert J.H. Miller*[1], Aakash Shanbhag*[2,3], Anna M. Michalowska[2], Paul Kavanagh[2], Joanna X. Liang[2], Valerie Builoff[2], Nowell M. Fine[1], Damini Dey[2], Daniel S. Berman[2], and Piotr J. Slomka[2]

[1]*Department of Cardiac Sciences, University of Calgary, Calgary, Alberta, Canada;* [2]*Departments of Medicine (Division of Artificial Intelligence in Medicine), Imaging, and Biomedical Sciences, Cedars-Sinai Medical Center, Los Angeles, California; and* [3]*Signal and Image Processing Institute, Ming Hsieh Department of Electrical and Computer Engineering, University of Southern California, Los Angeles, California*

Transthyretin cardiac amyloidosis (ATTR CA) is increasingly recognized as a cause of heart failure in older patients, with ^{99m}Tc-pyrophosphate imaging frequently used to establish the diagnosis. Visual interpretation of SPECT images is the gold standard for interpretation but is inherently subjective. Manual quantitation of SPECT myocardial ^{99m}Tc-pyrophosphate activity is time-consuming and not performed clinically. We evaluated a deep learning approach for fully automated volumetric quantitation of ^{99m}Tc-pyrophosphate using segmentation of coregistered anatomic structures from CT attenuation maps. **Methods:** Patients who underwent SPECT/CT ^{99m}Tc-pyrophosphate imaging for suspected ATTR CA were included. Diagnosis of ATTR CA was determined using standard criteria. Cardiac chambers and myocardium were segmented from CT attenuation maps using a foundational deep learning model and then applied to attenuation-corrected SPECT images to quantify radiotracer activity. We evaluated the diagnostic accuracy of target-to-background ratio (TBR), cardiac pyrophosphate activity (CPA), and volume of involvement (VOI) using the area under the receiver operating characteristic curve (AUC). We then evaluated associations with the composite outcome of cardiovascular death or heart failure hospitalization. **Results:** In total, 299 patients were included (median age, 76 y), with ATTR CA diagnosed in 83 (27.8%) patients. CPA (AUC, 0.989; 95% CI, 0.974–1.00) and VOI (AUC, 0.988; 95% CI, 0.973–1.00) had the highest prediction performance for ATTR CA. The next highest AUC was for TBR (AUC, 0.979; 95% CI, 0.964–0.995). The AUC for CPA was significantly higher than that for heart-to-contralateral ratio (AUC, 0.975; 95% CI, 0.952–0.998; $P = 0.046$). Twenty-three patients with ATTR CA experienced cardiovascular death or heart failure hospitalization. All methods for establishing TBR, CPA, and VOI were associated with an increased risk of events after adjustment for age, with hazard ratios ranging from 1.41 to 1.84 per SD increase. **Conclusion:** Deep learning segmentation of coregistered CT attenuation maps is not affected by the pattern of radiotracer uptake and allows for fully automatic quantification of hot-spot SPECT imaging such as ^{99m}Tc-pyrophosphate. This approach can be used to accurately identify patients with ATTR CA and may play a role in risk prediction.

Key Words: cardiac amyloidosis; technetium pyrophosphate; quantification; diagnostic accuracy; biomarker

J Nucl Med 2024; 65:1144–1150
DOI: 10.2967/jnumed.124.267542

Transthyretin cardiac amyloidosis (ATTR CA) is an increasingly recognized cause of heart failure (*1*). Bone scintigraphy imaging with tracers such as ^{99m}Tc-pyrophosphate has been established as a highly accurate tool for diagnosing ATTR CA, with initial studies describing evaluation of planar images alone (*2*). However, subsequent studies have shown potential pitfalls from using this approach (*3*). Visual evaluation of SPECT images, in combination with screening for light chain amyloidosis, has now become the gold standard for noninvasive diagnosis (*4*). SPECT imaging improves diagnostic accuracy but is inherently subjective and requires expertise.

Hybrid SPECT/CT imaging facilitates more robust methods to quantify myocardial radiotracer activity. Scully et al. demonstrated high diagnostic accuracy for quantitation using SUVs from regions placed manually on SPECT/CT images (*5*). In our previous work, we demonstrated that quantitative measures have high diagnostic accuracy (*6*) and correlate with native myocardial T1 (*7*). However, these techniques have not translated into clinical practice, at least in part because they require time-consuming manual segmentation. Recent developments in foundational deep learning models have made it feasible to segment cardiac chambers and ventricular myocardium from noncontrast, ungated CT images (*8*). These algorithms can be leveraged to automate and objectify the manual processes involved in quantifying radiotracer uptake in the myocardium in a robust manner that is not affected by the tracer uptake pattern. We developed this automated workflow for ^{99m}Tc-pyrophosphate uptake quantification and then evaluated the potential clinical utility of different approaches to quantitation.

MATERIALS AND METHODS

Study Population

In this retrospective study, we identified patients who underwent ^{99m}Tc-pyrophosphate SPECT/CT imaging at the University of Calgary between March 2020 and October 2022. For each patient with more than one ^{99m}Tc-pyrophosphate study, only the first study was included. Additionally, we excluded 7 cases with significant registration errors identified during quality control processes. Significant offset in any direction between rib or spine uptake and anatomic landmarks was considered misregistration. This study was reviewed and approved by the Institutional Review Board at the University of Calgary (REB19-1448), and the requirement to obtain informed consent was waived.

Clinical Data

Demographics, past medical history, and red flags for ATTR CA at the time of imaging were determined through manual review of

Received Jan. 29, 2024; revision accepted Apr. 3, 2024.
For correspondence or reprints, contact Piotr J. Slomka (piotr.slomka@cshs.org).
*Contributed equally to this work.
Published online May 9, 2024.

electronic medical records. Diagnosis of ATTR CA was based on the presence of, first, an endomyocardial biopsy positive for ATTR; second, diffuse myocardial uptake on SPECT/CT imaging after exclusion of monoclonal protein; or third, evidence of infiltrative cardiomyopathy on echocardiography or cardiac MRI with either a documented pathologic gene variant or a noncardiac biopsy demonstrating ATTR amyloidosis (*4,9*). One patient was diagnosed on the basis of the third criterion; this patient had undergone carpal tunnel biopsy (*10*) and showed mildly reduced biventricular function on cardiac MRI (genetic testing pending). At our center, coverage criteria for tafamidis initially required pathologic confirmation of disease, but this requirement was eventually removed to allow for noninvasive confirmation of diagnosis. An outline of patient diagnosis adjudication is shown in Supplemental Figure 1 (supplemental materials are available at http://jnm.snmjournals.org). All ATTR CA adjudication was performed with masking of the quantitative image results.

Imaging Protocols

Imaging with ^{99m}Tc-pyrophosphate was performed according to 1 of 2 protocols. All subjects underwent imaging on either an NM Discovery 870 (GE Healthcare, $n = 233$) or an NM Discovery 670 (GE Healthcare, $n = 63$) scanner. Patients received 740 MBq (20 mCi) of ^{99m}Tc-pyrophosphate, with planar images obtained at 3 h after injection over a 5- to 8-min duration, with a heart-centered field of view. SPECT images were acquired at 3 h with a 10% energy window and a 128 × 128 matrix. Patients imaged with the NM Discovery 870 had a total acquisition time of 12 min using a wide-energy, high-resolution collimator. Patients imaged with the NM Discovery 670 had a total acquisition time of 15 min using a low-energy high-resolution collimator. For both scanner systems, CT attenuation correction imaging was performed during an end-expiratory breath hold with no gating, in helical mode, with a slice thickness of 5 mm, tube voltage of 120 kVp and 20 mA, and a 512 × 512 matrix.

Expert Image Interpretation

Planar myocardial radiotracer retention was quantified from the 3-h images using heart-to-contralateral ratio at the time of clinical interpretation (*4*). Planar images at 3 h were also graded visually using Perugini grading (*2*). SPECT images at 3 h were visually assessed to determine whether diffuse radiotracer activity was present or absent in the myocardium (*4*).

CT Attenuation Correction Segmentation

A previously validated foundational deep learning model (Total Segmentator) was used to segment all heart chambers and myocardium (*11*). The model uses a no-new-Net (nnU-Net) architecture to automatically segment a variety of anatomic structures from CT images (*11*). A key advantage of this approach is the automatic optimization of the various hyperparameters, including an ensemble of 2- and 3-dimensional U-Net networks at multiple resolutions. For cardiac structures, the model was trained using expert annotations from contrast images, which were transferred to registered noncontrast images. We recently demonstrated excellent correlations between estimates from noncontrast CT and volumes manually segmented from gated, contrast-enhanced CT (left ventricular [LV] myocardium Spearman $r = 0.947$, LA volume Spearman $r = 0.926$) (*12*). The left atrium (LA) and LV myocardium, right atrium, and aorta regions derived automatically from the CT attenuation correction scans were then used to quantify the tracer on coregistered attenuation-corrected ^{99m}Tc-pyrophosphate SPECT images.

CT-Guided Quantification

All ^{99m}Tc-pyrophosphate quantification was performed using attenuation-corrected images. We used CT-derived LV myocardial boundaries to determine maximum myocardial counts. Maximum myocardial counts, corrected for radiotracer delay and camera sensitivity (*13*), were used to calculate the SUV_{max} from injected dose and weight (*14*). We also evaluated target-to-background ratio (TBR), as well as cardiac pyrophosphate activity (CPA) and volume of involvement (VOI), on the basis of our previous work (*6*). TBR is calculated as the maximum activity in the target (myocardium) divided by the mean activity of the background. VOI is quantified as the total volume of activity above threshold (maximum activity of the background) (*6*). CPA is quantified as the total activity (integrating volume and intensity) above threshold, divided by mean background activity (*6*).

For TBR, VOI, and CPA, LV myocardium was used as the target region, but we evaluated 5 methods for determining background activity. The first 3 methods were based on LA activity. First, we used the full cardiac segments to quantify LA ^{99m}Tc-pyrophosphate activity and LV myocardial ^{99m}Tc-pyrophosphate activity. These segmentations were used to quantify TBR_{full}, VOI_{full}, and CPA_{full}. Next, we evaluated a reduced-size left atrial region (reduced by 50%) to measure LA background activity. The reduced LA region was used to quantify TBR_{small}, VOI_{small}, and CPA_{small}. Lastly, we considered 5 regions of interests (200 mm^3 each) randomly sampled within the LA volume. This method was used to define TBR_{roi}, VOI_{roi}, and CPA_{roi} measures. Similarly, we used maximal uptake in the right atrium to derive TBR_{ra}, VOI_{ra}, and CPA_{ra} and maximal uptake in the aorta derive TBR_{aorta}, VOI_{aorta}, and CPA_{aorta}. Examples of the segmentation methods and overall deep learning workflow are shown in Figure 1.

Outcomes

The primary outcome was diagnostic accuracy for ATTR CA. In the secondary analysis, we evaluated associations with the combined

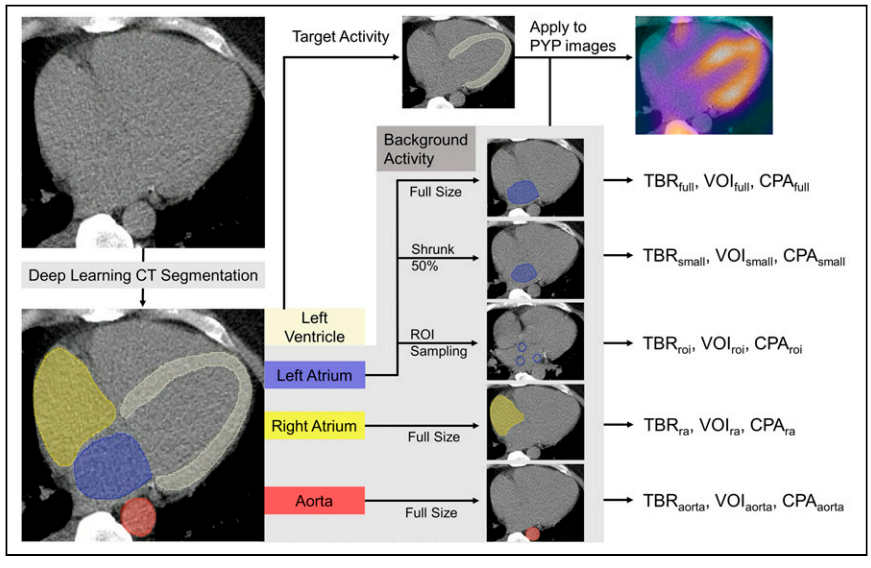

FIGURE 1. Overview of segmentation and image quantification. Deep learning was used to segment noncontrast CT scans. LV myocardium segmentation was used without modification. We evaluated 5 methods for determining background activity. LA was sampled with full region, reduced region (shrunk 50% but centered in LA), and random regions of interest. Right atrium and aorta were sampled with full-size volumes. These segmentations were used to calculate TBR, VOI, and CPA. PYP = ^{99m}Tc-pyrophosphate; ROI = region of interest.

clinical outcome of cardiovascular death or heart failure hospitalization. Admissions for heart failure were ascertained from electronic medical records based on a primary admitting diagnosis of heart failure using the standardized codes from the International Classification of Diseases, 10th revision (*15*). Cardiovascular mortality was ascertained from electronic medical records and included death related to heart failure, myocardial infarction, or sudden death (*16*). Follow-up was censored at the last time that follow-up status could be verified. Outcomes were adjudicated with masking of the ^{99m}Tc-pyrophosphate results.

Statistical Analysis

Categorical variables were summarized as numbers and percentages and compared with a χ^2 or Fisher exact test as appropriate. Continuous variables were summarized as mean and SD and compared using Student *t* test if normally distributed and summarized as median and interquartile range and compared using Wilcoxon rank sum test if not.

Prediction performance was evaluated using areas under the receiver operating characteristic curve (AUCs) and compared using the method of DeLong et al. (*17*). SPECT visual interpretation was not included in this analysis since it was used in part to adjudicate diagnosis. Unadjusted and age-adjusted associations with the combined outcome of cardiovascular death or heart failure hospitalization were assessed using Cox proportional hazards models. Multivariable models were limited to age-adjusted associations, given the low number of events (*18*). The proportional hazards assumption was assessed using Schoenfeld residuals, with no significant violations identified.

All statistical tests were 2-sided, with a *P* value of less than 0.05 considered statistically significant. All analyses were performed with STATA version 13 (StataCorp).

RESULTS

Patient Population

In total, 299 patients were included in the study, with a diagnosis of ATTR CA in 83 patients. The population characteristics are outlined in Table 1. Patients with ATTR CA were older (median age, 82 vs. 74 y; $P < 0.001$) and more likely to be male (81.9% vs. 56.5%; $P < 0.001$).

Cardiac chamber measurements took an average of 15.8 ± 0.2 s (including time for chamber segmentation and image quantification). Cases demonstrating chamber segmentation and image quantification are shown in Figure 2 for a patient with ATTR CA and in Figure 3 for a patient without ATTR CA. Imaging parameters are outlined in Table 2. The median SUV_{max}, TBR, VOI, and CPA, regardless of the quantification method, were significantly higher in patients with ATTR CA (all $P < 0.001$). Distributions of quantitative imaging variables are shown in Supplemental Figure 2.

Diagnostic Accuracy

Prediction performance for ATTR CA using clinical and quantitative measures, and using new automated measures with reduced LA volume as the background, is shown in Figure 4. CPA_{small} (AUC, 0.989; 95% CI, 0.974–1.00) and VOI_{small} (AUC, 0.988; 95% CI, 0.973–1.00) had the highest prediction performance for ATTR CA. The AUC for CPA_{small} was significantly higher than that for the heart-to-contralateral ratio (AUC, 0.975; 95% CI, 0.952–0.998; $P = 0.046$) and SUV_{max} (AUC, 0.944; 95% CI, 0.919–0.970; $P = 0.013$).

Prediction performance for ATTR CA using all automated methods for quantifying CPA is shown in Supplemental Figure 3. Of the quantification methods, CPA_{small} (AUC, 0.989; 95% CI, 0.974–1.00) and CPA_{ra} (AUC, 0.987; 95% CI, 0.970–1.00) had the highest prediction performance. Prediction performance for methods of quantifying TBR is shown in Supplemental Figure 4. Prediction performance using VOI, shown in Supplemental Figure 5, was similar to the results for CPA.

Clinical Outcomes

Among the 83 patients with ATTR CA, during a median follow-up of 1.6 y (interquartile range, 1.0–1.9 y), 15 patients experienced heart failure–related hospitalization and 8 patients experienced cardiovascular death as the first event. Unadjusted and age-adjusted associations with the combined outcome of cardiovascular death or heart failure hospitalization are shown in Figure 5. Most quantitative variables were associated with an

TABLE 1
Population Characteristics Stratified by Presence of ATTR CA

Characteristic	No ATTR CA ($n = 216$)	ATTR CA ($n = 83$)	*P*
Median age (y)	74 (IQR, 65–80)	82 (IQR, 72–86)	<0.001
Male (*n*)	122 (56.5%)	68 (81.9%)	<0.001
Medical history (*n*)			
Hypertension	152 (70.4%)	59 (71.1%)	0.900
Diabetes	56 (25.9%)	10 (12.0%)	0.010
Coronary artery disease	49 (22.7%)	20 (24.1%)	0.801
Atrial fibrillation	64 (29.6%)	37 (44.6%)	0.014
Amyloid red flags (*n*)			
Bilateral carpal tunnel syndrome	6 (2.8%)	41 (49.4%)	<0.001
Spinal stenosis	9 (4.2%)	15 (18.1%)	<0.001
Peripheral neuropathy	57 (26.4%)	46 (55.4%)	<0.001
Previous TAVI	6 (2.8%)	2 (2.4%)	0.852

IQR = interquartile range; TAVI = transcatheter aortic valve implantation.

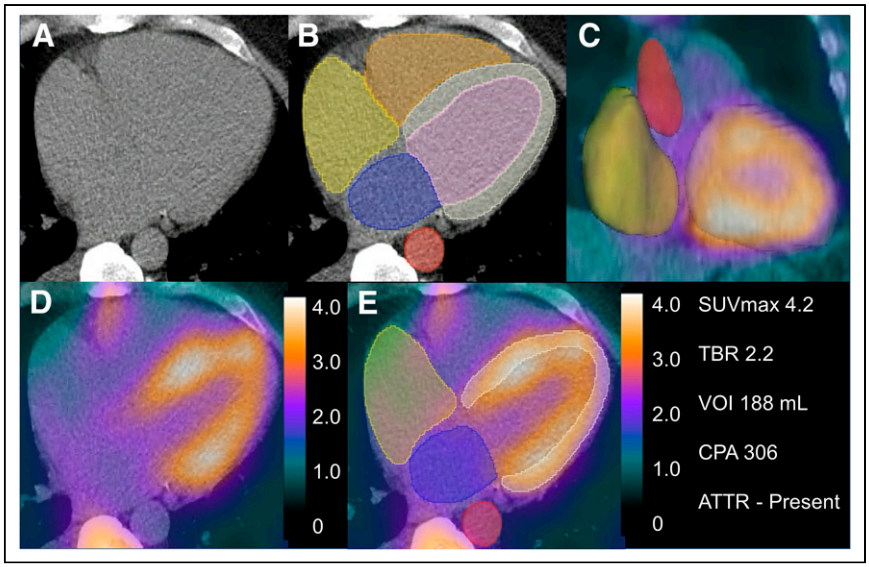

FIGURE 2. Example patient with ATTR CA. (A and B) Attenuation correction imaging (A) segmented using deep learning (B). (C) Three-dimensional segmentations for all chambers. (D) Hybrid SPECT/CT imaging, with scale in SUV. (E) Chamber segmentations applied to coregistered SPECT to quantify radiotracer activity.

increased risk of cardiovascular death or heart failure hospitalization in unadjusted analyses. After adjustment for age, all quantitative variables were associated with an increased risk of events, with hazard ratios ranging from 1.41 to 1.84 per SD increase.

DISCUSSION

We demonstrated the feasibility of fully automated quantification of ^{99m}Tc-pyrophosphate uptake using deep learning segmentation of coregistered CT attenuation maps. We leveraged CT anatomic information to identify structures that cannot be consistently identified using ^{99m}Tc-pyrophosphate imaging alone. The diagnostic accuracy for ^{99m}Tc-pyrophosphate quantification was consistently excellent, without the need for manual intervention. Quantification was independent of variability in ^{99m}Tc-pyrophosphate uptake, allowing quantification in cases with low uptake, where methods based on SPECT imaging alone may be subjective and unreliable. Lastly, we demonstrated the potential clinical importance of automated measures by evaluating associations with the combined outcome of cardiovascular mortality or hospitalization due to heart failure. Overall, our results suggest that fully automated quantitation of ^{99m}Tc-pyrophosphate is possible and could potentially be used to support physician interpretation or risk stratification.

There has been a significant increase in the use of ^{99m}Tc-pyrophosphate imaging in response to the high diagnostic accuracy of the test and increasing awareness regarding ATTR CA (*19*). As a result, ^{99m}Tc-pyrophosphate imaging is increasingly performed in community centers, where physicians may have less expertise in the technique. Although SPECT imaging is highly accurate when analyzed by experienced observers, experience is required to differentiate blood pool from myocardial radiotracer activity, particularly in cases with lower uptake. Dual-isotope imaging was proposed for quantifying myocardial uptake (*20*). However, this is currently impractical because of limited access to thallium, increased radiation exposure, and lack of a consistent definition of background activity. Hybrid SPECT/CT allows physicians to identify anatomic landmarks (*21*), so it is intuitive to use a similar approach for artificial intelligence approaches to image evaluation. We demonstrate the feasibility of this approach, using a deep learning model to segment CT attenuation imaging to facilitate automated quantification of SPECT tracer. A similar approach has been applied to whole-heart segmentation from CT attenuation correction imaging (*22*). Our method has the potential advantage of separating out regions of blood-pool activity from myocardial uptake and also providing the measures of overall disease burden such as CPA or VOI. Furthermore, the segmentation method for CT images was previously externally validated (*12*). Importantly, since the method is based on CT imaging, it does not rely on (or assume) any specific distribution of radiotracer. The model segments CT images rapidly (<16 s) and could be deployed as a preprocessing step, since the pipeline is fully automated. Therefore, it could be deployed in a clinical workflow without interruption to support physician interpretation, which may be particularly beneficial in centers without extensive ^{99m}Tc-pyrophosphate imaging expertise.

Several different methods for quantifying radiotracer ^{99m}Tc-pyrophosphate activity have been proposed to date. Scully et al.

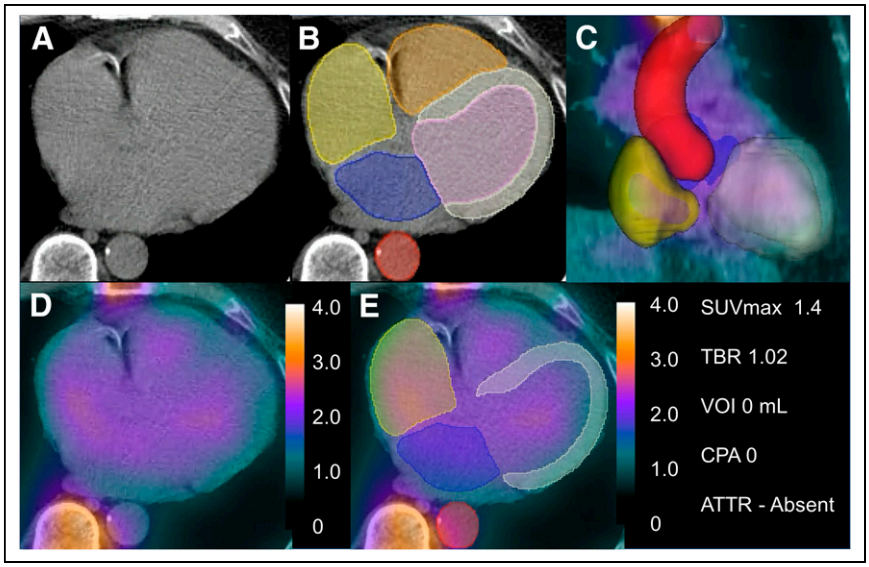

FIGURE 3. Example patient without ATTR CA. (A and B) Attenuation correction imaging (A) segmented using deep learning (B). (C) Three-dimensional segmentations for all chambers. (D) Hybrid SPECT/CT imaging, with scale in SUV. (E) Chamber segmentations applied to coregistered SPECT to quantify radiotracer activity.

TABLE 2
Imaging Characteristics Stratified by Presence of ATTR CA

Characteristic	No ATTR CA (n = 216)	ATTR CA (n = 83)	P
Clinical analysis			
Perugini grade 2/3 (n)	10 (4.6%)	80 (96.4%)	<0.001
HCL ratio	1.1 (1.0–1.2)	1.7 (1.5–1.9)	<0.001
SPECT visual positive (n)	0 (0.0%)	82 (98.8%)	<0.001
Quantitative analysis			
SUV_{max}	1.4 (0.5–1.7)	3.9 (2.8–5.7)	<0.001
TBR_{full}	1.18 (1.1–1.3)	2.1 (1.8–2.4)	<0.001
VOI_{full}	0 (0–0)	46.5 (13.7–71.0)	<0.001
CPA_{full}	0 (0–0)	74.7 (22.6–112)	<0.001
TBR_{small}	1.1 (1.0–1.3)	2.1 (1.8–2.4)	<0.001
VOI_{small}	0 (0–0)	67.2 (31.8–105)	<0.001
CPA_{small}	0 (0–0)	105 (46.2–177)	<0.001
TBR_{roi}	1.2 (1.1–1.3)	2.17 (1.8–2.4)	<0.001
VOI_{roi}	10.4 (2.9–28.1)	129 (91.3–166)	<0.001
CPA_{roi}	10.1 (3.0–27.5)	181 (120–235)	<0.001
TBR_{ra}	1.3 (1.2–1.5)	2.4 (2.1–2.9)	<0.001
VOI_{ra}	0 (0–0.2)	93.5 (47.0–130)	<0.001
CPA_{ra}	0 (0–0.2)	162 (84.3–233)	<0.001
TBR_{ao}	1.3 (1.2–1.5)	2.6 (2.3–3.3)	<0.001
VOI_{ao}	0 (0–0)	31.2 (5.9–63.9)	<0.001
CPA_{ao}	0 (0–0)	73.5 (12.3–154)	<0.001

HCL = heart to contralateral.
Continuous data are median and interquartile range.

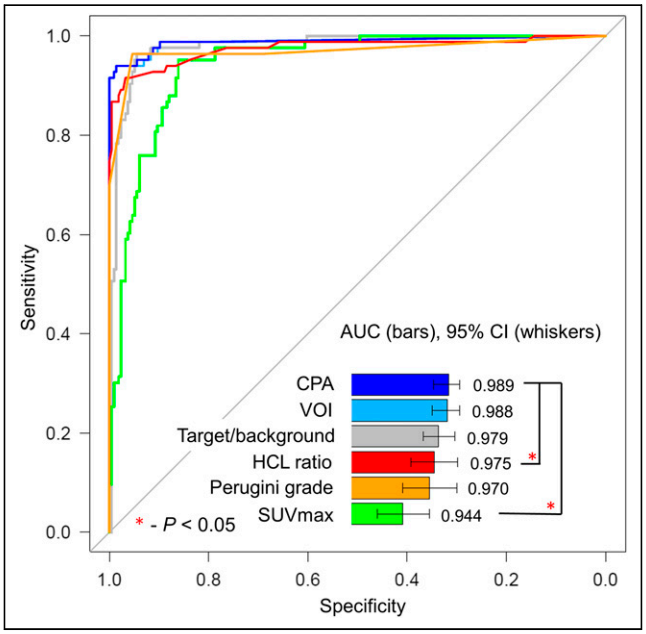

FIGURE 4. Prediction performance for diagnosis of ATTR CA using clinical and quantitative methods (n = 83/299). SUV_{max} was quantified from LV myocardium region. Background for TBR, CPA, and VOI was reduced-size region of interest in LA. HCL = heart to contralateral.

evaluated SUV_{peak} in myocardium as well as a retention index (*5*). Kessler et al. evaluated a method for whole-heart quantitation of radiotracer activity (*23*), which demonstrated high diagnostic accuracy. For quantifying cardiac amyloid activity, Dorbala et al. proposed a method that relied on manually defining myocardium on CT attenuation imaging and then transferring those contours to associated ^{99m}Tc-pyrophosphate imaging (*24*). Importantly, these measurements correlated strongly with cardiovascular MR markers of disease burden (*24*). In our previous work, we demonstrated that CPA and VOI (manually derived) have high diagnostic accuracy (*6*) and correlate with native myocardial T1 (*7*). However, all of those studies relied on tedious manual segmentation, which is a barrier to clinical translation.

We evaluated a large number of quantitation schemes facilitated by automated segmentation of CT structures. The diagnostic accuracy of most quantitative variables was excellent, with only a few significant differences identified. SUV_{max} had slightly lower diagnostic accuracy, which may be a reflection of inherent limitations in quantifying SUV from SPECT imaging (*25*) or of the fact that SUV_{max} is defined by a single pixel value. There was a trend toward higher prediction performance for methods using small LA volumes or RA volumes as background. All of the methods had diagnostic accuracy similar or superior to that of planar interpretation, which was informed by SPECT visual interpretation (since we relied on clinically reported planar interpretation). All of the methods for quantifying ^{99m}Tc-pyrophosphate activity from

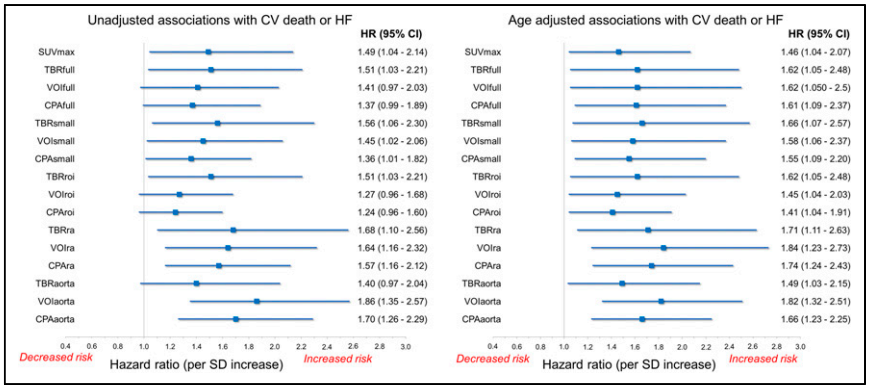

FIGURE 5. Associations (per SD increase) with incidence of cardiovascular (CV) death or heart failure (HF) hospitalization in patients with ATTR CA.

SPECT/CT were associated with the combined clinical outcome after adjustment for age. Further large-scale comparisons may be needed to differentiate more precisely between different methods of determining the background counts.

Identification of diffuse myocardial uptake on SPECT images is part of the diagnostic criteria for ATTR CA (*4*) but requires expertise to accurately differentiate blood pool from myocardium. Therefore, quantitative analysis of SPECT/CT may be particularly valuable in smaller centers, with less expertise, as a diagnostic tool. Furthermore, risk prediction remains an important clinical need, particularly with the emergence of additional therapies for ATTR CA (*26*). Objective and automated SPECT/CT quantification may identify patients at highest risk and also provide precise assessment of changes in radiotracer uptake in response to therapy (*27*). Artificial intelligence–based volumetric quantification of ^{99m}Tc-pyrophosphate activity, and potentially other bone-seeking radiotracers, may be a particularly precise way to follow changes in response to disease-modifying therapies (*28*). This could potentially be used to identify patients who are not responding to therapy and could be transitioned to other therapies.

Our study had a few important limitations. We quantified all SPECT/CT images at 3 h using ^{99m}Tc-pyrophosphate, and the results may not extrapolate to centers performing imaging only at 1 h (*3*) or using other radiotracers (*29*). Endomyocardial biopsy was not performed on most patients. Although a pathologic diagnosis would provide greater certainty regarding adjudication of ATTR CA, this is not reflective of clinical practice, which has shifted to increasingly noninvasive diagnosis (*3*). Additionally, we had a limited number of patients with serial studies and therefore were not able to assess changes over time or in response to therapy (*28*). However, this would be an important next step in evaluating this approach. Lastly, we relied on spatial registration between CT and ^{99m}Tc-pyrophosphate images. Expert oversight is needed to verify if the registration is correct, which may be difficult in cases with limited uptake. Nevertheless, correct SPECT/CT alignment is required for attenuation correction of the ^{99m}Tc-pyrophosphate counts, even if CT is not used for the region definition. Thus, any quantitative approach for attenuation-corrected ^{99m}Tc-pyrophosphate SPECT scans must ensure correct SPECT/CT registration.

CONCLUSION

The anatomic information available from CT attenuation correction imaging can be leveraged by deep learning to automatically segment and quantify ^{99m}Tc-pyrophosphate imaging regardless of the intensity or distribution of radiotracer uptake. This approach can be used to support physician interpretation of ^{99m}Tc-pyrophosphate images, which may be particularly beneficial in community centers, or to quantify radiotracer activity, which may potentially play a role in assessment of therapies or risk stratification.

DISCLOSURE

This research was supported in part by grant R35HL161195 from the National Heart, Lung, and Blood Institute/National Institutes of Health (NHLBI/NIH) (principal investigator, Piotr Slomka). The content is solely the responsibility of the authors and does not necessarily represent the official views of the National Institutes of Health. Robert Miller reports research and consulting support from Pfizer. Nowell Fine reports research and consulting support from Pfizer, Akcea, Alnylam, and Eidos. Paul Kavanagh, Daniel Berman, and Piotr Slomka participate in software royalties for QPS software at Cedars-Sinai Medical Center. Piotr Slomka has received research grant support from Siemens Medical Systems and consulting fees from Synektik. Daniel Berman has served as a consultant for GE Healthcare. No other potential conflict of interest relevant to this article was reported.

KEY POINTS

QUESTION: Can deep learning use anatomic information from CT attenuation maps to automatically quantify ^{99m}Tc-pyrophosphate imaging?

PERTINENT FINDINGS: Using 299 patients, we demonstrated the feasibility of a deep learning–based approach for quantifying ^{99m}Tc-pyrophosphate imaging, with a mean processing time of less than 16 s. Measures of ^{99m}Tc-pyrophosphate radiotracer uptake have high diagnostic accuracy for ATTR CA and were associated with the composite outcome of cardiovascular death or heart failure–related hospitalization.

IMPLICATIONS FOR PATIENT CARE: CT-guided quantification of ^{99m}Tc-pyrophosphate imaging can be used to automate analysis, support physician interpretation, and provide quantitative risk stratification.

REFERENCES

1. Ruberg FL, Grogan M, Hanna M, Kelly JW, Maurer MS. Transthyretin amyloid cardiomyopathy. *J Am Coll Cardiol.* 2019;73:2872–2891.
2. Perugini E, Guidalotti PL, Salvi F, et al. Noninvasive etiologic diagnosis of cardiac amyloidosis using ^{99m}Tc-3,3-diphosphono-1,2-propanodicarboxylic acid scintigraphy. *J Am Coll Cardiol.* 2005;46:1076–1084.
3. Masri A, Bukhari S, Ahmad S, et al. Efficient 1-hour technetium-99m pyrophosphate imaging protocol for the diagnosis of transthyretin cardiac amyloidosis. *Circ Cardiovasc Imaging.* 2020;13:e010249.
4. Dorbala S, Ando Y, Bokhari S, et al. ASNC/AHA/ASE/EANM/HFSA/ISA/SCMR/SNMMI expert consensus recommendations for multimodality imaging in cardiac amyloidosis. *J Nucl Cardiol.* 2020;27:659–673.
5. Scully PR, Morris E, Patel KP, et al. DPD quantification in cardiac amyloidosis. *JACC Cardiovasc Imaging.* 2020;13:1353–1363.
6. Miller RJH, Cadet S, Mah D, et al. Diagnostic and prognostic value of technetium-99m pyrophosphate uptake quantitation for transthyretin cardiac amyloidosis. *J Nucl Cardiol.* 2021;28:1835–1845.

7. Roshankar G, White GC, Cadet S, et al. Quantitative technetium pyrophosphate and cardiovascular magnetic resonance in patients with suspected cardiac amyloidosis. *J Nucl Cardiol.* 2022;29:2679–2690.
8. Han D, Shanbhag A, Miller RJH, et al. Artificial intelligence-based automated left ventricular mass quantification from non-contrast cardiac CT scans: correlation with contrast CT and cardiac MRI. medRxiv website. https://www.medrxiv.org/content/10.1101/2024.01.12.24301169v1. Published January 13, 2024. Accessed April 18, 2024.
9. Garcia-Pavia P, Rapezzi C, Adler Y, et al. Diagnosis and treatment of cardiac amyloidosis. A position statement of the European Society of Cardiology Working Group on Myocardial and Pericardial Diseases. *Eur J Heart Fail.* 2021;23:512–526.
10. Khayambashi S, Elzinga K, Hahn C, et al. Amyloidosis tissue confirmation for tafamidis eligibility using transverse carpal ligament and tenosynovium biopsy. *Can J Cardiol.* 2022;38:1643–1646.
11. Wasserthal J, Breit H-C, Meyer MT, et al. TotalSegmentator: robust segmentation of 104 anatomic structures in CT images. *Radiol Artif Intell.* 2023;5:e230024.
12. Miller RJ, Shanbhag A, Killekar A, et al. AI-defined cardiac anatomy improves risk stratification of hybrid perfusion imaging. *JACC Cardiovasc Imaging.* March 6, 2024 [Epub ahead of print].
13. Ito T, Matsusaka Y, Onoguchi M, et al. Experimental evaluation of the GE NM/CT 870 CZT clinical SPECT system. *J Appl Clin Med Phys.* 2021;22:165–177.
14. Kinahan PE, Fletcher JW. Positron emission tomography-computed tomography standardized uptake values in clinical practice and assessing response to therapy. *Semin Ultrasound CT MR.* 2010;31:496–505.
15. Southern DA, Norris CM, Quan H, et al. An administrative data merging solution for dealing with missing data in a clinical registry. *BMC Med Res Methodol.* 2008;8:1.
16. Hicks KA, Tcheng JE, Bozkurt B, et al. 2014 ACC/AHA key data elements and definitions for cardiovascular endpoint events in clinical trials. *J Am Coll Cardiol.* 2015;66:403–469.
17. DeLong ER, DeLong DM, Clarke-Pearson DL. Comparing the areas under two or more correlated receiver operating characteristic curves. *Biometrics.* 1988;44:837–845.
18. Austin PC, Steyerberg EW. Events per variable (EPV) and the relative performance of different strategies for estimating the out-of-sample validity of logistic regression models. *Stat Methods Med Res.* 2017;26:796–808.
19. Poterucha TJ, Elias P, Bokhari S, et al. Diagnosing transthyretin cardiac amyloidosis by technetium Tc 99m pyrophosphate: a test in evolution. *JACC Cardiovasc Imaging.* 2021;14:1221–1231.
20. Tamarappoo B, Otaki Y, Manabe O, et al. Simultaneous Tc-99m PYP/Tl-201 dual-isotope SPECT myocardial imaging in patients with suspected cardiac amyloidosis. *J Nucl Cardiol.* 2020;27:28–37.
21. Sperry BW, Bateman TM, Akin EA, et al. Hot spot imaging in cardiovascular diseases. *J Nucl Med.* 2022;63:1722–1740.
22. Bhattaru A, Rojulpote C, Vidula M, et al. Deep learning approach for automated segmentation of myocardium using bone scintigraphy SPECT/CT in patients with suspected cardiac amyloidosis. *J Nucl Cardiol.* 2024;33:101809.
23. Kessler L, Fragoso Costa P, Kersting D, et al. Quantitative ^{99m}Tc-DPD-SPECT/CT assessment of cardiac amyloidosis. *J Nucl Cardiol.* 2023;30:101–111.
24. Dorbala S, Park MA, Cuddy S, et al. Absolute quantitation of cardiac (99m)Tc-pyrophosphate using cadmium-zinc-telluride-based SPECT/CT. *J Nucl Med.* 2021;62:716–722.
25. Dickson JC, Armstrong IS, Gabiña PM, et al. EANM practice guideline for quantitative SPECT-CT. *Eur J Nucl Med Mol Imaging.* 2023;50:980–995.
26. Maurer MS, Kale P, Fontana M, et al. Patisiran treatment in patients with transthyretin cardiac amyloidosis. *N Engl J Med.* 2023;389:1553–1565.
27. Fontana M, Martinez-Naharro A, Chacko L, et al. Reduction in CMR derived extracellular volume with patisiran indicates cardiac amyloid regression. *JACC Cardiovasc Imaging.* 2021;14:189–199.
28. Papathanasiou M, Kessler L, Bengel FM, et al. Regression of myocardial ^{99m}Tc-DPD uptake after tafamidis treatment of cardiac transthyretin amyloidosis. *J Nucl Med.* 2023;64:1083–1086.
29. Hutt DF, Quigley AM, Page J, et al. Utility and limitations of 3,3-diphosphono-1,2-propanodicarboxylic acid scintigraphy in systemic amyloidosis. *Eur Heart J Cardiovasc Imaging.* 2014;15:1289–1298.